

# Magnetic reconnection and plasmoid formation in three-dimensional accretion flows around black holes

Antonios Nathanail<sup>1,4\*</sup>, Vasilis Mpisketzis<sup>1</sup>, Oliver Porth<sup>2</sup>, Christian M. Fromm<sup>3,4,5</sup>, and Luciano Rezzolla<sup>4,6,7</sup>

<sup>1</sup>*Department of Physics, National and Kapodistrian University of Athens, Panepistimiopolis, GR 15783 Zografos, Greece*

<sup>2</sup>*Astronomical Institute Anton Pannekoek, Universiteit van Amsterdam, Science Park 904, 1098 XH, Amsterdam, The Netherlands*

<sup>3</sup>*Institut für Theoretische Physik und Astrophysik, Universität Würzburg, Emil-Fischer-Strasse 31, 97074 Würzburg, Germany*

<sup>4</sup>*Institut für Theoretische Physik, Goethe Universität Frankfurt, Max-von-Laue-Str.1, 60438 Frankfurt am Main, Germany*

<sup>5</sup>*Max-Planck-Institut für Radioastronomie, Auf dem Hügel 69, D-53121 Bonn, Germany*

<sup>6</sup>*School of Mathematics, Trinity College, Dublin 2, Ireland*

<sup>7</sup>*Frankfurt Institute for Advanced Studies, Ruth-Moufang-Str. 1, 60438 Frankfurt am Main, Germany*

11 May 2022

## ABSTRACT

Magnetic reconnection is thought to be one of the main energy-dissipation mechanisms fueling energy to the plasma in the vicinity of a black hole. Indeed, plasmoids formed through magnetic reconnection may play a key role in  $\gamma$ -ray, X-ray and near-infrared flares from the black hole at the center of our galaxy, SgrA\*. We report the results of three-dimensional general-relativistic ideal and resistive magnetohydrodynamics simulations modelling magnetic reconnection in accretion flows around astrophysical black holes. As an important difference with similar works, our accretion discs have an initial dipolar magnetic-field configuration with loops of alternating polarity. We show that current sheets are formed and destroyed rapidly in the turbulent environment of black-hole accretion. Plasmoids are formed from current sheets close to the event horizon, in a region of  $\sim 2 - 15$  gravitational radii. We further quantify the magnetic dissipation and the process of energy transfer to the plasmoids, reporting the reconnection rate, the relative current density with respect to the local magnetic field, and the size of the plasmoids. We find that plasmoids gain energy through reconnection and heat up to relativistic temperatures, with the largest ones being sufficiently energetic to leave the black hole near the polar regions. During their evolution, plasmoids are stretched and elongated, becoming disrupted when the shear is sufficiently large, although some plasmoids survive as well-distinguished structures at distances of  $\sim 30 - 40$  gravitational radii from the black hole. Finally, we find that in some cases the plasmoids acquire a super-Keplerian azimuthal velocity, as suggested by recent observations of flares from Sgr A\*.

**Key words:** black hole physics, accretion, accretion discs, magnetic reconnection, magnetohydrodynamics

## 1 INTRODUCTION

The supermassive black hole in the Galactic center, Sgr A\*, is the closest of its kind and is the subject of several campaigns of multi-wavelength observations since it is an excellent laboratory for accretion physics in the extreme-gravity regime. Over the years, unparalleled insight on the accretion flow in the immediate environment of the central black hole has been obtained (Falcke et al. 1998; Doeleman et al. 2008; Dodds-Eden et al. 2009; Reid 2009; Johnson & Gwinn 2015; Broderick et al. 2016). On a daily basis bright flares in the X-rays and in the near-infrared (NIR) are observed (Baganoff et al. 2001; Genzel et al. 2003; Marrone et al. 2007;

Witzel et al. 2018). It has been suggested that flares may be the result of magnetic reconnection in the vicinity of the central black hole (Markoff 2005; Broderick & Loeb 2006; Yuan et al. 2009; Barrière et al. 2014; Haggard et al. 2019). Flares are observationally associated with an increase of almost two orders of magnitude in the typical NIR emission (Ponti et al. 2017; Do et al. 2019), but such an increase is difficult to be accounted for in terms of a significant change in the accretion flow (Ressler et al. 2018). On the other hand, orbital motion originated at the inner edge of the accretion flow, around the supermassive black hole, Sgr A\*, was recently detected from the GRAVITY collaboration et al. (2018), thus leading support to the idea that localised emission does take place in the accretion flow.

\* E-mail: antonionitoni@hotmail.com, anathanail@phys.uoa.gr

Promising phenomenological models that match the overall

observables of Sgr A\* (see, e.g., Yuan et al. 2003) lack the detailed description of the accretion flow and must be enhanced with theoretical description of the flaring activity observed in Sgr A\*. The latter can be accomplished by incorporating magnetic reconnection as a channel to dissipate the magnetic energy and naturally give rise to localised emission, modeled as hot-spots or plasmoids, and ultimately leading to the observed flares (Broderick & Loeb 2005; Dodds-Eden et al. 2010; Younsi & Wu 2015; Ball et al. 2016; Li et al. 2017a; Gutiérrez et al. 2019; Gravity Collaboration et al. 2020).

Global simulations can accurately describe the accretion dynamics but lack the detailed microphysical description of particle acceleration in the current sheets that are formed and abruptly destroyed close to the event horizon. Large current sheets of alternating magnetic-field polarity have been found to be very efficient in particle acceleration. More specifically, the initial magnetic field tends to fragment at the location of the current sheet and subsequently produces chains of magnetic “plasmoids” or “magnetic islands” (Loureiro et al. 2007; Uzdensky et al. 2010; Fermo et al. 2010; Huang & Bhattacharjee 2012; Loureiro et al. 2012; Takamoto 2013). We recall that plasmoids are magnetic-flux bundles, which, in the absence of a bulk motion, may become quasi-spherical blobs due to a fast tearing instability; these blobs then contain and trap charged particles that can be accelerated to relativistic energies. Overall, plasmoids are characterised by possessing a rather large magnetisation  $\sigma := B^2/\rho$ , that is, a large ratio between the magnetic –  $B := \sqrt{B^i B_i}$  is the magnetic-field strength, with  $B^i$  the magnetic-field components – and the rest-mass energies. A phenomenological cutoff of  $\sigma \gtrsim 0.3$  was found in two-dimensional (2D) general-relativistic magnetohydrodynamics (GRMHD) in the ideal limit (Nathanail et al. 2020a; Ripperda et al. 2020), a result that is consistent with local, particle-in-cell (PIC) simulations (Sironi et al. 2016; Li et al. 2017b; Kagan et al. 2018; Petropoulos et al. 2018, 2019). Indeed, although restricted to microscopical scales, PIC simulations have provided a significant insight in the process of magnetic reconnection in current sheets, where plasmoids and plasmoid chains are naturally accelerated and produce distributions of non-thermal electrons (Sironi & Spitkovsky 2014; Guo et al. 2014; Guo et al. 2015; Werner et al. 2016; Rowan et al. 2017; Ball et al. 2018b; Rowan et al. 2019; Guo et al. 2021; Zhang et al. 2021).

The global picture of the reconnection processes taking place in the turbulent accretion environments near a black hole can be drawn only by exploiting accurate and long-term GRMHD simulations (Chan et al. 2015; Dexter et al. 2009; Dodds-Eden et al. 2010; Ball et al. 2016; Dexter et al. 2020; Porth et al. 2021; Ripperda et al. 2021). Such simulations have recently provided a significant boost to the study and understanding of the occurrence and on the impact that magnetic reconnection has in accretion flows (Ball et al. 2018a; Qian et al. 2018; Kadowaki et al. 2018; Vourellis et al. 2019; White et al. 2020; Čemeljić et al. 2020; Dihingia et al. 2021; Chashkina et al. 2021; Scepi et al. 2021). In particular, the production of energetic plasmoids that tend to orbit in the vicinity of the black hole were observed in high-resolution GRMHD simulations both in the ideal limit (Nathanail et al. 2020a) – in which case the resistivity is purely of numerical origin – and in general-relativistic resistive (GRRMHD) simulations – where the resistivity is instead physical (Ripperda et al. 2020).

These studies confirmed the expectation that plasmoids are generated close to the event horizon from magnetic reconnection events. The plasmoids can have a size of a few gravitational radii and the “reconnection rate” – which is defined in terms of the ra-

tio between the velocity of the plasma inflowing into the current sheet and that leaving the sheet – was found to be between 0.01 and 0.03 (Ripperda et al. 2020) confirming previous relativistic studies, both numerical and analytic (Del Zanna et al. 2016; Ripperda et al. 2019b; Bhattacharjee et al. 2009; Uzdensky et al. 2010). The production of plasmoids in the simulation does not alter or enhance the variability of the accretion flow, but it may be responsible for observed variability (or even flaring) in the NIR or the X-rays (Nathanail et al. 2020a). After they are formed, plasmoids can steadily acquire additional energy through continued magnetic reconnection, as they evolve and cool down. Moreover, in an accretion flow originating from a disc, plasmoids have in general a non-zero angular momentum and hence can potentially be related to observations of orbiting hot spots near the galactic center (GRAVITY collaboration et al. 2018).

In our previous work in which we have analysed the production and evolution of plasmoids in accretion flows onto black holes (Nathanail et al. 2020a), the restriction to a 2D setup and thus the assumption of axisymmetry has prevented us from a direct comparison with the observations. Furthermore, the simulations by Nathanail et al. (2020a) could not capture the development of non-axisymmetric instabilities that affect both the production, but, more importantly, the evolution of the plasmoids. The most important aspect of this evolution is that plasmoids, as they move outwards from the vicinity of the black hole, are stretched and elongated, sometimes even being disrupted when the shear is sufficiently large.

We here present the results of three-dimensional (3D) GRMHD simulations of magnetic reconnection in the vicinity of a black hole. More specifically, discuss and compare the same simulation setup when explored solving either the equations of GRMHD either in the ideal MHD limit or in the presence of a finite and physical resistivity. In both cases, we find that the production of plasmoids and of plasmoid chains is comparable and similar to one obtained in the 2D simulations of Nathanail et al. (2020a). On the other hand, the 3D simulations also reveal important differences in the evolution of the plasmoids, which can become considerably stretched in the azimuthal direction as a result of the accretion process in the disc. Furthermore, the plasmoids produced in the simulations attain after a few crossing times  $t_g := r_g/c := GM/c^3$  – where  $G$  is the gravitational constant,  $M$  the mass of the black hole,  $c$  the speed of light and  $r_g$  the gravitational radius – a high azimuthal velocity which can be well super-Keplerian and have an elongated structure extending over  $\pi/10$  radian. Interestingly, Matsumoto et al. (2020) have found that a better fit for the observed flare from the galactic source Sgr A\* is obtained when modelling the circular orbit via a super-Keplerian motion.

The structure of the paper is the following: In Section 2 we present the details of our simulations, with subsection 2.1 presenting the numerical setup is discussed and subsection 2.2 reporting the details of the accretion process. The results of the simulations are instead discussed in Section 3, with subsection 3.1 detailing the evolution of the disc and the magnetic field, while subsections 3.2 and 3.4 report on the analysis of the plasmoid-formation processes and on their dynamics, respectively. Finally, we conclude and provide a brief summary discussion of our results in Section 4.

## 2 MAGNETIC RECONNECTION IN 3D ACCRETION FLOWS: SETUP

### 2.1 Numerical setup

The numerical setup consists of a Kerr black-hole spacetime and of an initially perturbed torus seeded with a poloidal magnetic field. All simulations presented here are performed in three spatial dimensions employing the general-relativistic MHD code BHAC (Porth et al. 2017), which uses second-order shock-capturing finite-volume methods and has been employed in several investigations (Nathanail et al. 2019; Mizuno et al. 2018; Nathanail et al. 2020b). The code uses the constrained-transport method (Del Zanna et al. 2007), in order to preserve a divergence-free magnetic field (Olivaes et al. 2019), and has been thoroughly tested and compared with GRMHD codes of similar capabilities (Porth et al. 2019).

Our initial data consist of an equilibrium torus with constant specific angular momentum  $\ell = 4.28$  (Fishbone & Moncrief 1976), orbiting around a Kerr black hole with three dimensionless spins, i.e.,  $a = 0, 0.5$  and  $0.95$ . The inner and outer radii of the torus are at  $r_{\text{in}} = 6r_g$  and  $r_{\text{out}} = 12r_g$  respectively, whereas the outer boundary of the computational domain lies at  $500r_g$ .

As mentioned above, initially the torus is seeded with magnetic field which is purely poloidal, and consists of a series of nested loops with varying polarity (i.e., the magnetic field in neighbouring loops has a clockwise direction, which is then followed by a counter-clockwise one when seen in a vertical cross-sectional plane). The respective vector potential has the form:

$$A_\phi \propto \max\left(\frac{\rho}{\rho_{\text{max}}} - 0.2, 0\right) \cos((N-1)\theta) \sin\left(\frac{2\pi(r-r_{\text{in}})}{\lambda_r}\right), \quad (1)$$

where the maximum rest-mass density in the torus is denoted with  $\rho_{\text{max}}$  and the additional parameters ( $N \geq 1$  and  $\lambda_r$ ) set the number and the characteristic length-scale of the initial loops in the torus. For the results presented here, we consider only models with  $N = 3$  and  $\lambda_r = 2$ . Similar magnetic-field configurations have been thoroughly presented and analysed in the force-free limit in 2D and 3D (Parfrey et al. 2015; Yuan et al. 2019a,b; Mahlmann et al. 2020).

The computational domain uses spherical logarithmic Kerr-Schild coordinates covering  $r \in [0.88r_g, 500r_g]$ ,  $\theta \in [0, \pi]$  and  $\phi \in [0, 2\pi]$  with a base resolution of  $N_r \times N_\theta \times N_\phi = 192 \times 192 \times 96$  cells. By exploiting BHAC’s adaptive mesh-refined capabilities, two additional sub-grids are introduced in those regions where magnetic reconnection is expected to be efficient, and plasmoid production occurs. As a result, a second level is placed within a radius of  $3 < r/r_g < 30$  and a third level is placed at  $5 < r/r_g < 20$ . Compared to the reference case from Porth et al. (2019), which simulates a larger radial extent of  $2500r_g$ , the resulting effective resolution in the regions of prime interest is hence  $N_r \times N_\theta \times N_\phi = 1050 \times 768 \times 384$ .

For the three ideal-GRMHD models (see Table 1), dissipation of the magnetic energy is entirely numerical and, as was shown in 2D simulations, physically meaningful results can nevertheless be obtained when exploring the behaviour of the solution with increasing resolution (Obergaullinger et al. 2009; Rembiasz et al. 2017; Nathanail et al. 2020a; Obergaullinger & Aloy 2020). For the simulation run that has physical resistivity, i.e., for model HB.res.0.9, we solve the resistive GRMHD equations in the version implemented in BHAC (Ripperda et al. 2019a), and we assume a uniform and constant resistivity with a rather small value of  $\eta = 5 \times 10^{-5}$ . The small resistivity is chosen in order to reproduce

**Table 1.** Initial parameters for the models considered. The second column refers to the dimensionless spin of the black hole, whereas the third to the initial average magnetisation in the torus. The last column corresponds to the module used in BHAC Ideal or Resistive. Each model name (in the first column) encodes information of the model parameters.

model	$a$	$\langle\sigma_{\text{init}}\rangle$	module
HB.id.0.0	0.0	$10^{-5}$	Ideal
HB.id.0.5	0.5	$10^{-5}$	Ideal
LB.id.0.0	0.0	$10^{-4}$	Ideal
HB.res.0.9	0.9	$10^{-5}$	Resistive
HB.id.0.9	0.9	$10^{-5}$	Ideal

a near-ideal limit for the accretion flow dynamics, but also to allow for a physical reconnection that will result in plasmoid formation (Ripperda et al. 2019b, 2020). When assuming the gravitational radius,  $r_g$ , as the typical lengthscale, the chosen resistivity results in a large lundquist number of  $S := r_g c/\eta = 10^4$ , that is, the minimum lundquist number needed to produce plasmoids under the physical conditions considered here (Bhattacharjee et al. 2009; Uzdensky et al. 2010; Ripperda et al. 2019b, 2020).

### 2.2 Properties of the accretion flow

The main focus of our work is the magnetic reconnection occurring close to event horizon and the production of plasmoids through this process. However, we need to analyze the main properties of the accretion dynamics through the mass-accretion rate and the magnetic flux across the horizon. We measure the former as

$$\dot{M} := \int_0^{2\pi} \int_0^\pi \rho u^r \sqrt{-g} d\theta d\phi, \quad (2)$$

and we report its behaviour as function of time in the upper panel of Fig. 1 for all of the tori considered. Note that, after a time of  $\sim 3000M$ , the accretion process reaches a quasi-steady state till the end of the simulation for all models, thus highlighting that a stationary turbulent state – produced by the development and saturation of the magnetorotational instability (MRI) – is sustained in the torus.

The magnetic flux accreted across the event horizon is instead defined as

$$\Phi_{\text{BH}} := \frac{1}{2} \int_0^{2\pi} \int_0^\pi |B^r| \sqrt{-g} d\theta d\phi, \quad (3)$$

while the “normalized” magnetic flux  $\phi_{\text{BH}} := \Phi_{\text{BH}}/\sqrt{\dot{M}}$  is shown in the lower panel of Fig. 1 for all of the models considered. To better distinguish the evolution of the magnetic flux of different polarity, we perform the integrals by considering separately the positive and the negative  $B^r$  component in one hemisphere. This is shown in Fig. 2, which reports how there is no magnetic flux threading the horizon initially. However, as accretion is triggered, both polarities are dragged in and the flux of positive  $B^r$  (blue dashed line) becomes slightly larger than the corresponding negative one. However, as the evolution proceeds, also the flux of negative  $B^r$  (red dashed line) increases, reaching levels that are comparable to the positive one. Overall, once stationarity is reached, the two fluxes are fluctuating but comparable, as one would expect in a situation where large amounts of reconnection takes place.

We recall that the most extensively investigated modes of disc accretion onto a black hole are either of SANE (Standard And Normal Evolution) (Narayan et al. 2012), or MAD (Magnetically

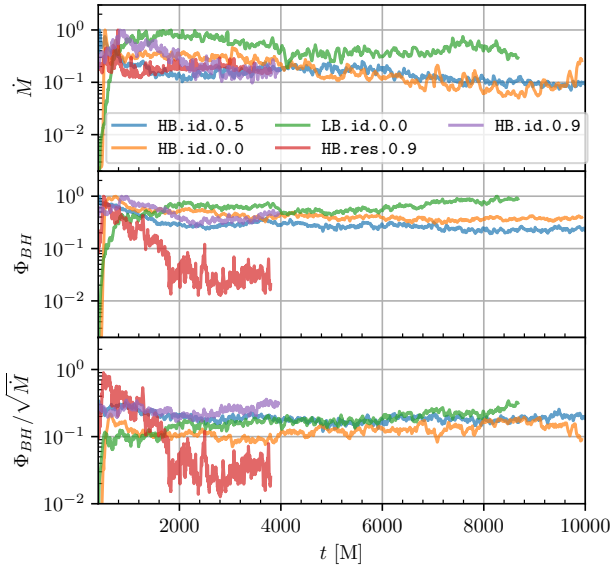


**Figure 1.** Upper panel: evolution of the mass-accretion measured across the black hole event horizon. Middle panel: evolution of the magnetic flux accreted onto the black hole. Lower panel: evolution of the normalized magnetic flux accumulated on the black-hole horizon. Different lines refer to the different models considered and summarised in Table 1.

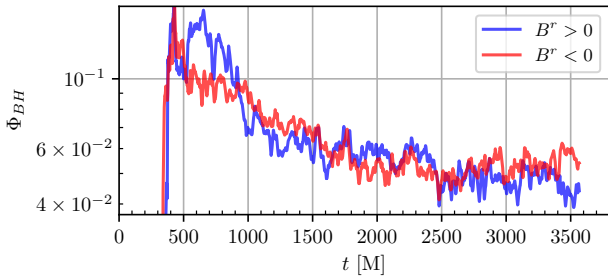


**Figure 2.** Evolution of the magnetic flux accreted onto the black hole over one hemisphere for model `HB.id.0.5`. The blue shaded line corresponds to a magnetic flux of positive polarity (i.e., the integrated flux with  $B^r > 0$ ) and red dashed line to the other polarity (i.e., integrated flux with  $B^r < 0$ ).

Arrested Disc) (Igumenshchev et al. 2003) type. Among the various differences in their properties (see, e.g., Event Horizon Telescope Collaboration et al. 2019a), possibly the most salient one is given by the typical value of the normalised flux, which is around  $\phi_{\text{BH}} = \phi_{\text{max}} \approx 15$  (within the units adopted here which matches the limiting flux quoted by Tchekhovskoy et al. (2011)) for a MAD accretion. In particular, a MAD state can be obtained when the accretion of magnetic flux onto the event horizon is sufficiently high to reach equipartition with the disc ram pressure and possibly even counter accretion (Igumenshchev et al. 2003). In this respect, the models considered here do not acquire a significant magnetic flux during their evolution and hence cannot be considered as MAD accretion discs. On the other hand, they cannot be considered SANE accretion discs either, since these are produced with tori having nested loops of one polarity and are therefore characterised by magnetized funnels with a much lower normalized magnetic flux and a much lower jet power (Event Horizon Telescope Collaboration et al. 2019a; Wong et al. 2021). The initial magnetic-field configuration and the size of the torus are the most important parameters

for the resulting evolution. A large-scale toroidal magnetic field, with a rather high initial magnetization, has been shown to produce powerful jets (Christie et al. 2019). During such evolutions, however, the global large-scale magnetic polarity can change sign and so does the magnetic flux across the event horizon. This behaviour is different from what reported here, where the magnetic flux across the event horizon can change sign (even on small timescales; see Fig. 2), but where the global large-scale magnetic field always admits both polarities, which are therefore susceptible to intense reconnection. A change of sign of the radial magnetic field component in the evolution of the accretion flow was observed in Barkov & Baushev (2011), where the initial magnetic-field configuration had two large magnetic loops of different polarity. From the analysis reported by Barkov & Baushev (2011), it seems that first a jet of one polarity was established and then, as magnetic flux of different polarity was accreted, the jet was destroyed and re-established.

We believe the reason why our accretion discs do not fall in either of the two classes is because our initial magnetic-field topology results in a fluctuating accretion of magnetic flux. More specifically, magnetic flux of one polarity is brought to the event horizon of the black hole, and as the magnetic flux of the opposite polarity reaches the vicinity of the horizon, they annihilate reducing the overall flux across the event horizon. In this way, no stable jet can be produced and indeed this what the simulations reveal. In addition, another distinctive feature of our accretion flows is that there is no need to reset to atmosphere values in the regions within the funnel. This is because the funnel is neither depleted of plasma, nor reaches high values of magnetisation, as instead happens in the case of MAD and SANE accretion discs.

We measure the energy released from the outflow through the energy flux that passes through a 2-sphere placed at  $r = 50 r_g$  and compute it as

$$\dot{E} := \int_0^{2\pi} \int_0^\pi (-T_t^r - \rho u^r) \sqrt{-g} d\theta d\phi, \quad (4)$$

the integrand in Eq. (4) is set to zero when surface  $\sigma \leq 1$  (Porth et al. 2019). The energy of the outflow in code units and normalized with the mass-accretion rate is shown in the upper panel Fig. 3. Note that the evolution of the energy of the outflow shows large fluctuations and for some models (e.g., `HB.id.0.0`) these fluctuations are of more than two orders of magnitude larger. To better understand which part of the outflow is giving most of the energy, we explore the jet and counter jet (upper/lower) asymmetry measuring the asymmetry of the outflow and the contribution from the upper and lower (above and below the black hole) via the parameter  $\mathcal{P}$  defined as follows (Nathanail et al. 2020a)

$$\mathcal{P} := \frac{\dot{E}_u - \dot{E}_l}{\dot{E}_u + \dot{E}_l}, \quad (5)$$

where  $\dot{E}_u$  and  $\dot{E}_l$  are the power of the upper and lower part of the outflow, respectively. Clearly, when the upper jet dominates  $\mathcal{P} \simeq 1$ , and when the lower jet dominates  $\mathcal{P} \simeq -1$ , while when  $\mathcal{P} \simeq 0$  the jets are symmetric [we set  $\mathcal{P} = 0$  whenever  $\sigma < 1$  in expression (4)]

The inspection of the lower panel of Fig. 3 reveals that for all models there is no steady emission from the upper or the lower part of the outflow. More specifically, the zero spin model `HB.id.0.0` switches its emission in the upper and lower vertical directions with higher periodicity than the spinning  $a = 0.5$  model `HB.id.0.5`. Furthermore, for the  $a = 0$  model `HB.id.0.0`, a low jet power is measured and indeed expected on the basis of the very small values of the magnetic flux accreting onto the black hole in this

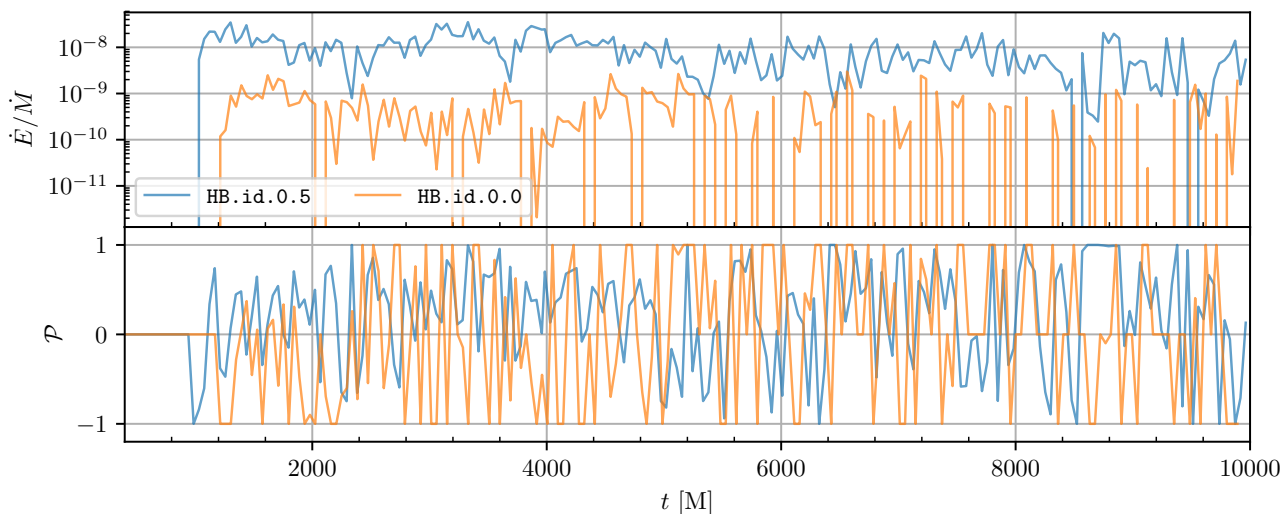


**Figure 3.** Upper panel: evolution of the power of the outflow when normalized by the mass-accretion rate; note that the energy of the outflow shows large fluctuations and for nonrotating black holes (model HB.id.0.0) these are of more than two orders of magnitude larger than for rotating ones. Lower panel: evolution of the north/south asymmetry in the jet as defined in Eq. (5); note that for all models there is no steady emission from the upper or the lower part of the outflow.

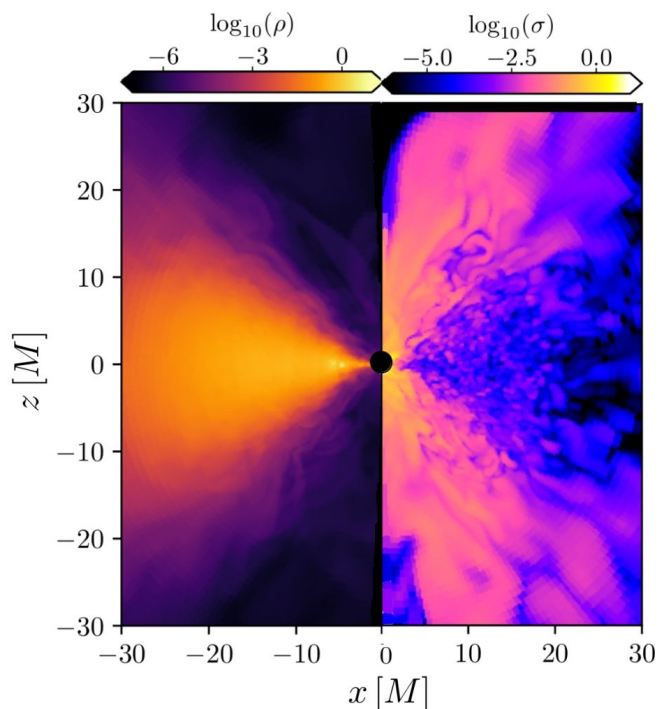


**Figure 4.** Distribution of the rest-mass density (left part) and of the magnetisation (right part) for model HB.id.0.5. Note the typical presence of a low-density funnel where the magnetisation can acquire higher values.

case. Note that for clarity Fig. 3 reports the behaviour of only two representative models but the behaviour illustrated is shared across all of the models considered.

### 3 MAGNETIC RECONNECTION IN 3D ACCRETION FLOWS: RESULTS

#### 3.1 Disc and Magnetic field evolution

VLBI (Very Large Baseline Interferometry) imaging of supermassive black holes on scales comparable with that of the event horizon requires a detailed knowledge of the physical environment near the black hole and is essential in distinguishing between theoretical models of the plasma condition and different types of compact objects (Mizuno et al. 2018; Event Horizon Telescope Collaboration et al. 2019a,b; Olivares et al. 2020). Similarly, polarization measurements can give more insight in the magnetic field structure and its activity, together with microphysics of emission, such as the production of an electron population with a non-thermal energy distribution (Event Horizon Telescope Collaboration et al. 2021a,b; Goddi et al. 2021; Mizuno et al. 2021). Finally, probing the topology of the magnetic field can be also essential for understanding flaring activity (GRAVITY collaboration et al. 2018).

Our simulations reveal that, as the accretion onto the black hole tends to a quasi-stationary state, the magnetisation tends to rise significantly in the low-density funnel region and provides conditions that are favourable for an efficient plasmoid production. This can be seen in Fig. 4, where we report the rest-mass density (left part) of the matter both in the torus (where is very high) and in the funnel region, where it is considerably reduced. Also shown with a different colorcode is the magnetisation (left part), which is instead very large in the funnel.

The central black hole absorbs the plunging matter that has arrives on the event horizon via the development of the MRI and in doing so has advected large amounts of magnetic field. Inside the torus, the magnetic field is mostly chaotic as a result of the highly turbulent motion there; however, as it reaches the funnel region, it becomes more and more twisted due to the disc rotation and, in the case of rotating black holes, also the spacetime rotation induced by the dragging of inertial frames. However, even for black holes with a zero spin, a similar magnetic field topology is observed, since the field lines are twisted mostly because of the motion of the fluid.

Thanks to our initial magnetic-field with poloidal loops of al-

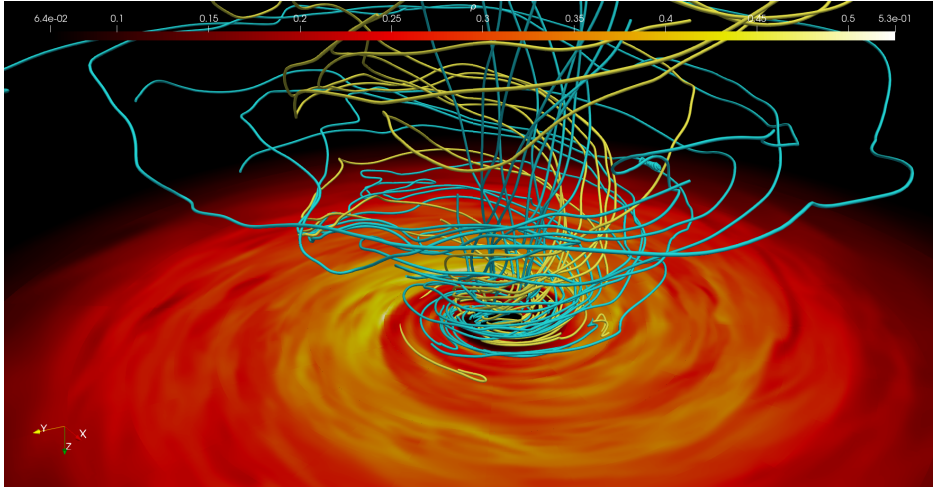


**Figure 5.** Three-dimensional representation of the accretion flow and of the magnetic-field topology. The rest-mass density distribution is shown only in the equatorial plane with a yellow-red colorcode. Shown instead with cyan and yellow colours are the magnetic-field lines of different polarity that will lead to reconnection and plasmoid formation in the funnel. The data refers to the rotating black-hole model `HB.id.0.5`.

ternating polarity, a very specific magnetic-field configuration is produced in the funnel region, as shown in Fig. 5, where magnetic-field lines – mostly of poloidal nature – and of different polarity are depicted with cyan and orange colour, respectively. These field lines are rooted near the event horizon and it is clear that the three-dimensional interfaces where these lines intersect in the high-magnetisation funnel are potential reconnection sites. Configurations of this type could be relevant for production of striped jets – that is, a jet with alternating toroidal magnetic-field polarity along the propagation axis – especially if the initial magnetic field is strong and thus leading to more powerful outflows (Gianios & Uzdensky 2019). More importantly, the reconnection sites produced by this magnetic-field configuration with poloidal magnetic fields having alternating polarities are quite different from the reconnection sites found at the funnel wall, which have lower magnetisation – both for SANE and MAD accretion modes – or from the reconnection taking place on the equatorial current sheet. Indeed, in typical single-loop initial magnetic fields, plasmoid production occurs almost exclusively at the edge of the jet funnel, that is, the jet sheath and not inside the funnel, which is instead filled with highly magnetized material and poloidal magnetic-field lines of the same polarity that produce a powerful outflow.

In Fig. 5 we have masked the torus above and below the equatorial plane so as to better visualise the magnetic-field topology, leaving the rest-mass density visible only near the equatorial plane in order to illustrate the motion of the fluid. This representation clearly highlights that determining the launching sites of magnetic reconnection have an intrinsically 3D nature and that any 2D representation would inevitably provide only a limited view, albeit still correct (Nathanail et al. 2020a; Ripperda et al. 2020). This limitation of 2D simulations becomes particularly severe in those conditions – such those encountered in our simulations – where the accretion flow is particularly variable and chaotic.

### 3.2 Plasmoids: physical conditions at generation

Current sheets are formed everywhere inside the torus due to the turbulent nature of the magnetic field there. However, because of the large rest-mass density and the small magnetisation in the torus,

the efficiency of magnetic reconnection in such regions is rather low and hence reconnection does not heat the local plasma significantly. On the other hand, the efficiency of magnetic reconnection is expected to be rather high at the funnel sheath, where the rest-mass density decreases and there is a significant gradient in the magnetisation, which increases moving towards the polar axis.

Inside the funnel, the magnetic-field lines are sheared and twisted (as seen in Fig. 5) due to differential rotation of the accreting fluid. Reconnection of these flux tubes releases magnetic energy that heats up the plasma close to relativistic temperatures, with values of the dimensionless temperature that can be as large as  $\Theta_e := p/\rho \approx 0.1$  in those regions where plasmoids are generated. Furthermore, a portion of the plasmoids produced in this way can reach energies sufficiently large to become gravitationally unbound, although this does not necessarily imply that the plasmoids will actually reach spatial infinity as some of them are actually moving inwards and are therefore accreted by the black hole.

In Fig. 6 we present some representative snapshots portraying the production of a large-scale plasmoid from model `LB.id.0.0` when represented in a 2D slice at  $\phi = 0$ . The upper and lower rows refer respectively to times  $t = 2860 M$  and  $t = 2950 M$  and have been selected to illustrate how a time interval of less than  $100 M$  is sufficient to build a large plasmoid with a radius of  $\approx 3 - 5 r_g$ . Note that the reconnecting current sheets produce filaments of small plasmoids – or plasmoid chains – which, over time, merge leading to a single large plasmoid that spirals and moves outwards in this case.

More specifically, the first column of panels in Fig. 6 show the Bernoulli parameter  $hu_t$  at different times – where  $h$  is the specific enthalpy and  $u_t$  the time covariant component of the fluid four-velocity (Rezzolla & Zanotti 2013). When  $hu_t < -1$ , this quantity can be used to distinguish fluid elements that are gravitationally unbound as a result of the energization through reconnection, and which can in principle leave the black hole. The second column of panel shows instead the vertical component of the magnetic field,  $B^z$ , using a colourcode that emphasises the different polarities. In this way, it is possible to highlight the reconnecting current sheet on the left part of the plot, where the layer of blue regions (negative polarity) lies inside the red area (positive polarity). In the third

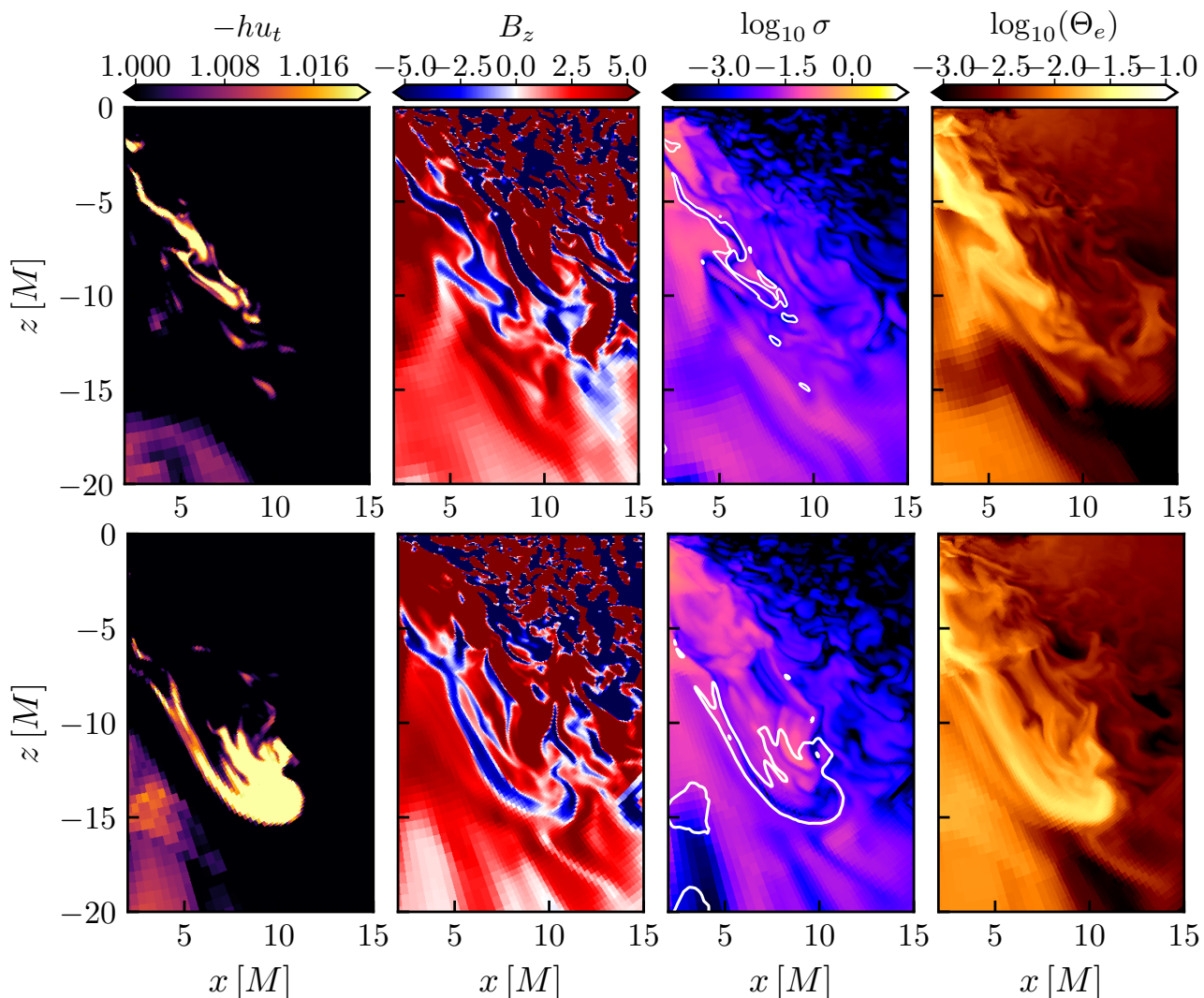


**Figure 6.** Two-dimensional section at  $\phi = 0^\circ$  showing the production of a plasmoid. From left to right, the four panels report: the Bernoulli parameter  $-hu_t$ , the vertical magnetic-field component  $B^z$ , the magnetisation scalar  $\sigma$ , and the dimensionless temperature  $\Theta_e$ . The data refers to the ideal-MHD model LB.i.d.0.0 at time  $t = 2860 M$  in the upper panels and at  $t = 2950 M$  in the lower panels.

column we report the magnetisation parameter  $\sigma$ , which shows that exactly at the location of the current layer, the magnetisation has decreased due to occurrence of reconnection. Finally, the last column presents the dimensionless temperature  $\Theta_e$ , highlighting how this increases as a result of reconnection. We note that reconnection with mild magnetisation,  $\sigma \approx 0.1 - 1$  results in a significant heating of the plasmoid, with relativistic temperatures  $\Theta_e \approx 0.1$ . Such plasmoids can power episodic outflows as the accretion takes place.

A rather important aspect of the plasmoid-formation process that we have not yet discussed about is the presence of a considerable azimuthal motion in the plasmoids formed in our simulations. Hence, in addition to the intrinsic and background azimuthal motion of the accreting plasma (Shende et al. 2019), plasmoids produced in 3D simulations can acquire an additional and considerable acceleration in the azimuthal direction when produced via reconnection. It is important to note here that plasmoids are significantly affected by the local guide field (Edmondson & Lynch 2017) and, indeed, episodic magnetic reconnection, such as break-out reconnection, has been observed in the solar corona (Kumar et al. 2019).

A similar process can be thought to take place also in this accretion scenario, as the plasma enters the funnel region and reconnecting current sheets can efficiently accelerate plasmoids and generate particles with energy distributions that are non-thermal and which we do not model here.

We have already introduced that reconnection layers with high lundquist numbers are unstable to the plasmoid instability and result in fast magnetic reconnection with a high reconnection rate, which becomes essentially independent of the value of the plasma resistivity (Bhattacharjee et al. 2009; Uzdensky et al. 2010; Stanier et al. 2019; Ripperda et al. 2020). This process – and in particular the weak dependence of the reconnection rate on the resistivity once a sufficiently high lundquist number has been achieved – has been shown to be present also in the case of turbulent reconnection (Lazarian et al. 2020). In our resistive model HB.res.0.9, we find that the lundquist number is high enough, namely  $S \gtrsim 10^4$ , that the plasmoid instability is triggered. In this model, for which we solve the equations of GRRMHD, magnetic reconnection and energy dissipation is a result of physical resistivity. In this way, we can analyse in a consistent (although not necessarily realistic)

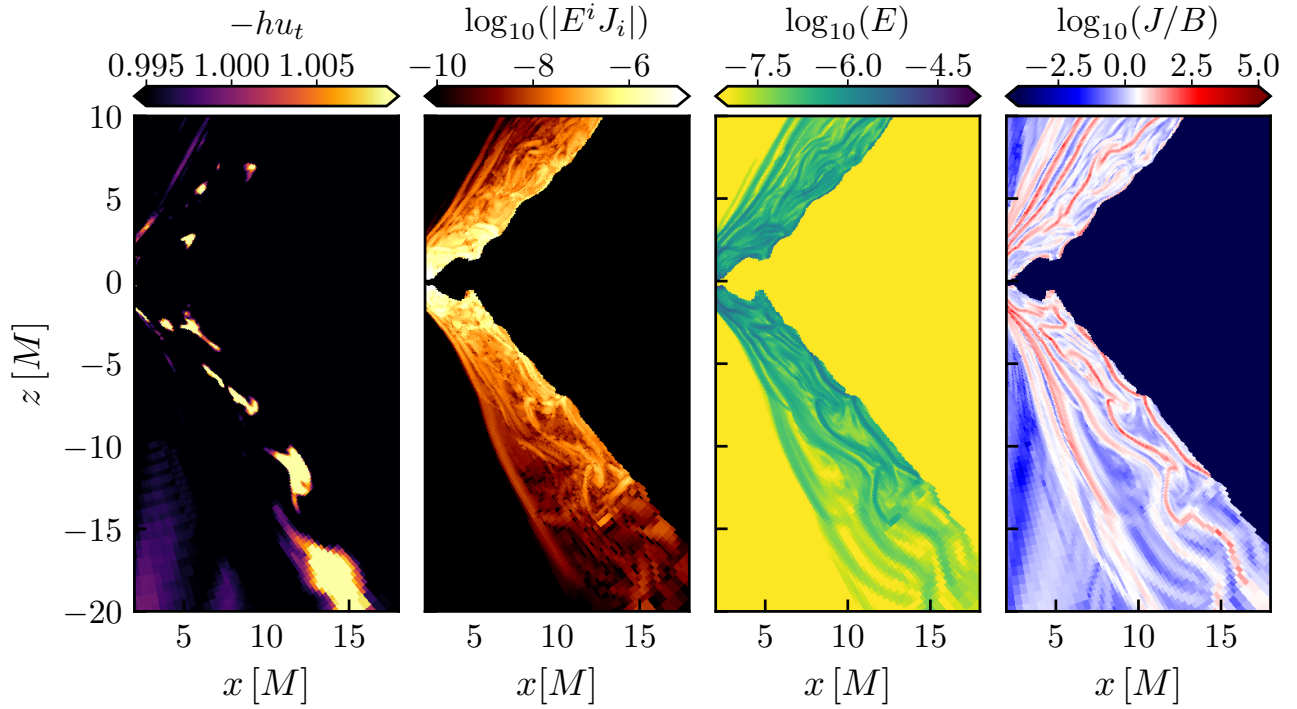


**Figure 7.** Two-dimensional section at  $\phi = 0^\circ$  showing the production of a plasmoid. From left to right, the four panels report: the Bernoulli parameter  $-hu_t$ , the magnitude Ohmic heating  $\log_{10}(|E^i J_i|)$ , the electric-field strength  $\log_{10}(E)$ , and the the ratio between the electric current density and the magnetic-field strength  $\log_{10}(J/B)$ . The data refers to the resistive-MHD model HB.res.0.9 at time  $t = 1130 M$ ; note that the high-density region in the torus is masked.

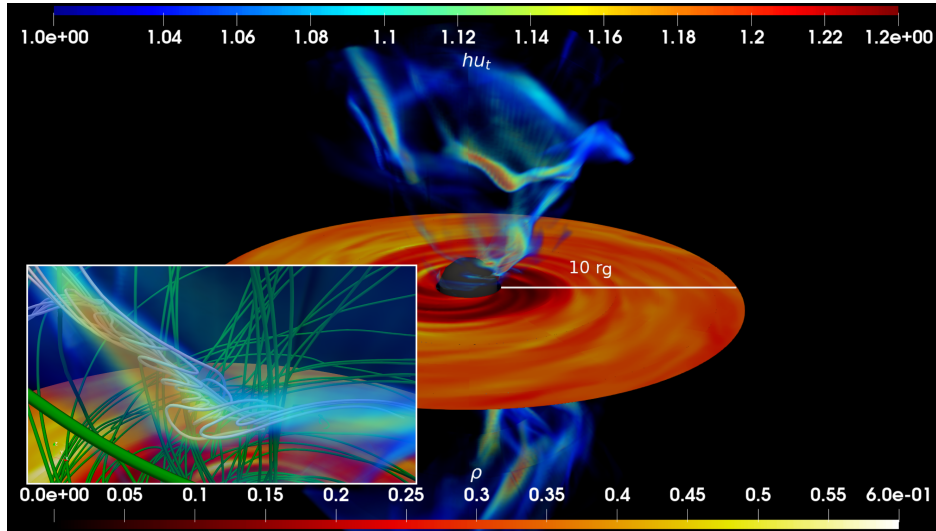


**Figure 8.** Three-dimensional view of the magnetisation for model LB.id.0.0 and at time  $4200 M$ . Note that the rest-mass density is shown only on the equatorial plane so as to have a sense of the rotation in the torus, The colourcode for the magnetisation is chosen to range between 1.00 and 1.20, so that those regions with  $\sigma \gtrsim 1.15$  effectively represent a plasmoid. The small box offers a zoomed view of the largest plasmoid of the snapshot; magnetic field outside the plasmoid are shown in green, while those inside the plasmoid as shown in cyan.

manner the Ohmic heating taking place during the reconnection events and also monitor the properties and evolution of the electric field. Moreover, through this model, we can perform a close comparison between the ideal-MHD and the resistive-MHD simulations we have performed.

Figure 7 reports a plasmoid chain produced at  $t = 1130 M$

in the resistive model HB.res.0.9. In the first panel we show again the Bernoulli parameter  $hu_t$  and in the in subsequent panels we mask the high-density region of the torus in order to highlight the important regions outside the torus where magnetic reconnection is most efficient. In particular, in the second panel we show in a logarithmic scale the magnitude Ohmic heating  $E^i J_i$ , where

$E^i$  and  $J^i$  are the components of the electric field and current, respectively. Note that the Ohmic heating is significant at the layer entering the funnel and peaks close to the black hole event horizon. Furthermore, this strong parallel electric field can efficiently accelerate particles close to the event horizon, but also along the sheath of the funnel region which has a width of  $\approx 5 r_g$ . As a result of these accelerations, the energy distribution of the electrons involved can deviate significantly from a thermal distribution Mizuno et al. (2021).

The third panel, on the other hand, shows the magnitude of the electric field, which clearly peaks there where the current-sheet layers develop. Finally, the fourth panel reports the ratio between the electric current density  $J := \sqrt{J^i J_i}$  and the magnetic-field strength  $J/B$ , that again traces the reconnecting current layers at the sheath of the funnel region. Note that at the current sheets the electric current  $J$  can be between two and three orders of magnitude larger than the magnetic field  $B$ .

Also in the case of the resistive simulation, larger plasmoids with a width of a few  $r_g$  are produced in the over a timescale of about  $100 M$ , as already observed in the ideal-MHD simulations. This allows us to estimate the reconnection rate to be  $\approx 0.01$ , which hints to the occurrence of fast magnetic reconnection consistent with the high lundquist number associated with our model (Bhattacharjee et al. 2009; Uzdensky et al. 2010; Ripperda et al. 2019b). Finally, the ability to model also a magnetic field allows us to estimate the inflow velocity of the current sheets in terms of the radial drift velocity,  $(\vec{E} \times \vec{B})^r / B^2$ , for which can measure in the neighbourhood of the current sheets a value of  $|(\vec{E} \times \vec{B})^r / B^2| \approx 10^{-2}$ .

All things considered, the evolution of the resistive model and the plasmoids formed in the corresponding accretion flow are rather similar to the ideal runs we have performed. Most probably this is due to the small resistivity used, which is however essential in order to model the accretion dynamics accurately and avoid excessive magnetic diffusion in the torus. As a way to improve our resistive-MHD description, we could employ a non-uniform resistivity so as to reproduce a physical scenario consisting of a low-resistivity torus and of a highly resistive funnel close to the event horizon. An approach following the one suggested by Dionysopoulou et al. (2015) will be explored in a future work.

### 3.3 Plasmoids: launching sites and morphology

We have so far concentrated on the processes giving rise and providing energy to the plasmoids found in our simulations. Next, we will discuss in detail where these plasmoids are produced, what are the main features of their dynamics as they interact with the background shearing flow, and how they can be related with the flaring activity seen in the supermassive black hole at the center of our galaxy, Sgr A\*.

Already in Sec. 3.1 we have illustrated that reconnection is very active in the low-density funnel as a result of poloidal flux tubes of alternating polarity that interact and reconnect. Most of the time, large plasmoids produced in these regions do not fall back to the black hole, but continue in an outward motion. These plasmoids are different from those that are produced well inside the torus and whose origin is linked to the turbulent motion triggered by the development of the MRI. These other plasmoids, which are created as frequently as they are destroyed, do not lead to a significant increase of the temperature of the disc, mostly because of the very low magnetisation in the dense interior of the torus. A third and final launching site of plasmoids is represented by the jet sheath, that

is, the thin vertical region of rapid increase of the magnetisation placed between the torus and the jet interior.

The spatial distribution of the magnetisation can be used to determine the plasmoid launching sites and deduce their 3D morphology. As already noted by Nathanail et al. (2020a), the magnetisation is extremely large within a current sheet (or filament in 2D simulations) although it can drop to zero at the center of the sheet, where the magnetic field vanishes and changes sign (see Fig. 8 in Nathanail et al. 2020a). In view of this, we provide in Fig. 8, which provides a 3D view of the magnetisation for model LB.id.0.0 and at time  $4200 M$ . Note that in the figure we have masked the rest-mass density above and below the equatorial plane, visualising it only on the equatorial plane so as to have a sense of the rotation in the torus (the radius of the disc is  $30 r_g$ ). The colourcode for the magnetisation is chosen to range between 1.00 and 1.20, so that those regions with  $\sigma \gtrsim 1.15$  can be considered to be representing a plasmoid.

Concentrating on features above the equatorial plane, it is possible to recognise at least two distinct plasmoids, with an approximate size of  $\sim 10 - 15 r_g$  along the filament and a diameter of  $\sim 3 - 5 r_g$ . The first one is near the event horizon and at lower latitudes, while the second one is further away from the event horizon and at higher latitudes. Note that their shape is far from spherical and both plasmoids appear mostly as filaments and with an orientation that is either mostly poloidal (first plasmoid) or a combination of poloidal and toroidal (second plasmoid). Hence, the morphology of plasmoids in 3D simulations is rather different from the one that can be deduced from 2D simulations, where they appear mostly as spherical. In particular, the 3D rendering allows one to appreciate that the shearing present in the background flow inevitably introduces a toroidal component in the plasmoid morphology.

From a statistical point of view, plasmoids of smaller size, i.e.,  $4 - 6 r_g$  along the filament and a diameter of  $\sim 2 - 3 r_g$ , are produced very frequently and over a timescale of  $10 - 20 M$ . However, they are either accreted by the black hole, or they are quickly destroyed by the shear (see the blue clouds in Fig. 8). Much more infrequently, i.e., over a timescale of  $\approx 500 - 700 M$ , plasmoids with larger size, i.e.,  $10 - 15 r_g$ , are generated and are thus able to survive for longer times as clearly identifiable compact features. Furthermore, also in the case of large plasmoids, their fate is to be dissolved rather quickly. Indeed, in none of our simulations, plasmoids are found to survive outside a spherical region of  $\approx 30 r_g$  from the event horizon. Beyond this region, in fact, all plasmoids have been converted to high-temperature clouds that cool down with time.

### 3.4 Plasmoids: dynamics and flares

After having described where plasmoids are produced and their morphology over time, it is now interesting to examine the possibility that these plasmoids – especially when they have sufficiently large energies and orbit outwards around the black hole – can be associated with the flares observed in Active Galactic Nuclei (AGN) (Yuan et al. 2009; Giannios 2013; Younsi & Wu 2015; Li et al. 2017a).

To this scope, the first important step is to locate and track the trajectories followed by the plasmoids as they move outwards. This task, however, is not trivial and far more demanding than in 2D simulations, where the reduced dimensionality allows one first to find a plasmoid and then track over time their evolution (see, e.g., Fig. 9 in Nathanail et al. 2020a).

In a 3D simulation, on the other hand, plasmoids also have

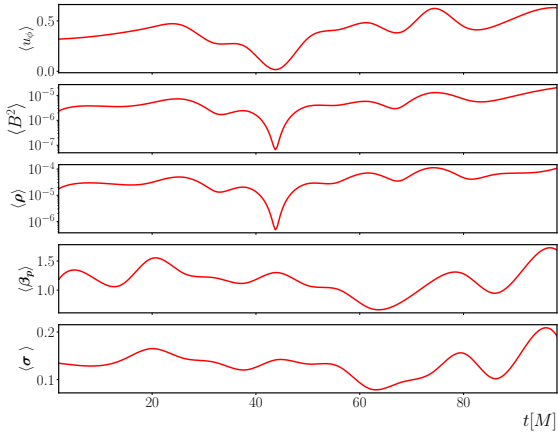


**Figure 9.** Evolution of volume-averaged characteristic physical quantities around the unbound plasmoid; shown from top to bottom are the azimuthal velocity  $u_\phi$ , the magnetic-field energy, the rest-mass density, the plasma parameter  $\beta_p$ , and the magnetisation  $\sigma$ . Note that the corresponding averaged quantities in the funnel are orders of magnitude smaller; the data refers to model HB.id.0.5.

an azimuthal motion and hence require a full 3D reconstruction of their motion. In order to monitor the evolution of the plasmoids as a whole, we compute averages over volumes containing the most energetic regions of the plasma and compute there the evolution of the most relevant physical quantities in the low-density funnel (see Fig. 9). Using model LB.id.0.0 as a reference, we monitor the evolution of the most energetic plasmoids, i.e., with  $hu_t < -1.1$ , and follow their evolution for a timescale of  $\approx 1000 M$ , which corresponds to a bit more than  $\approx 330$  min when for a black hole with a mass as that of Sgr A\*.

Figure 9 reports the evolution of the most energetic plasmoids, i.e., with  $hu_t > 1.01$ , in terms of volume-averaged quantities<sup>1</sup> such as (from top to bottom): the azimuthal component of the four-velocity  $u_\phi/c$ , the magnetic-field energy, the rest-mass density, the plasma parameter  $\beta_p := p_g/p_{\text{mag}}$  (i.e., the ratio between the fluid and magnetic pressures) and the magnetisation around the plasmoid. Note that the azimuthal velocity reaches values of  $> 0.5 c$ , which exceeds the local Keplerian velocity from a radius of  $\approx 3 r_g$  and further out.

These energetic plasmoids can be very good candidates to explain the observed orbital motions during flares from Sgr A\* (GRAVITY collaboration et al. 2018; Matsumoto et al. 2020). Another important aspect of the super-Keplerian plasmoids is that they get energised continuously, as seen from the magnetic-field strength, the temperature and magnetisation evolution (shown in the second, fourth and fifth row of Fig. 9 respectively). At the same time, the whole of the plasma in the funnel slow down in the azimuthal direction, and tent to lose their magnetisation, which however, was low from the beginning.

<sup>1</sup> For each scalar quantity  $\Phi$ , we define the corresponding volume average over the unbound material as  $\langle \Phi \rangle := \int_{hu_t > 1.0} \Phi dV / \int_{hu_t > 1.0} dV$ . Note that this is reasonable because the region with  $hu_t > 1.0$  has a compact support.

## 4 CONCLUSIONS

We have reported on three-dimensional GRMHD simulations of accretion flows onto rotating black holes, either in the ideal-MHD limit or with a finite physical resistivity. In all cases, the initial accretion flow is produced by a magnetised MRI unstable torus which is seeded with poloidal loops of alternating polarity. Using these simulations, we have shown that magnetic reconnection in the vicinity of an astrophysical black hole can efficiently produce macroscopic filamentary plasmoids with an approximate length of  $\sim 10 - 15 r_g$  and a diameter of  $\sim 3 - 5 r_g$ . They are generated approximately every  $\approx 500 - 700 M$ , and do not survive as compact structures outside a spherical region of  $\approx 30 r_g$  from the event horizon. Plasmoids of smaller size, i.e., with a length of  $4 - 6 r_g$  and a diameter of  $\sim 2 - 3 r_g$ , are produced more frequently and over a timescale of  $10 - 20 M$ . However, they are either quickly destroyed by the shear or accreted by the black hole.

Plasmoids can acquire large azimuthal velocities, exceeding the local Keplerian velocity. Moreover, after their formation they can retain their magnetisation or even increase it thanks to a continuous transfer of energy through reconnection or the coalescence with other plasmoids. In this way, they can be heated-up to relativistic temperatures,  $\Theta_e \approx 0.1 - 1$ . During the evolution of the accretion flow, multiple current sheets are formed inside the disc. However, due to the low magnetisation, and the high density, this is not so efficient and only locally insignificantly heats the plasma.

Interestingly, the overall evolution of the resistive model was found to be close to the corresponding model evolved in the ideal-MHD limit, with the exception of a lower variability in the accretion flow. Monitoring the production of large-scale plasmoids, we could estimate indirectly a reconnection rate of  $\approx 0.01$  and measure the current density reaching values  $J/B > 10^{2-3}$  in current sheets generated in the jet sheath. In these regions, the local drift velocity was also found to be  $|(\vec{E} \times \vec{B})^r / B^2| \approx 10^{-2}$ .

Flaring activity and intense variability has been observed in AGNs and Sgr A\*, which hints to very rapid particle acceleration in a compact region of a few gravitational radii (Levinson 2007; Begelman et al. 2008; Ghisellini & Tavecchio 2008; Giannios et al. 2009). Magnetic reconnection in the vicinity of a black hole can thus provide both requirements for an AGN flare. Our simulations can set the base for such an analysis with underlying realistic magnetic reconnection in general relativity and full 3D. Furthermore, the generic behaviour of the release of magnetic energy in the vicinity of a black hole can have implications to low accretion radiatively inefficient flows such as Sgr A\*. The compact radio source at the center of our galaxy has been observed with frequent flares increasing more than two orders of magnitude from the usual flux (Ponti et al. 2017; Do et al. 2019). Plasmoids produced in the models of our study have shown a similar activity, and at times where macroscopic plasmoids are formed, they acquire high azimuthal velocities which makes them potential candidates to match and explain observations of orbiting hot spots near the galactic center by the (Abuter et al. 2018).

Finally, we note that the analysis of how the plasmoids produced in simulations of this type would lead to VLBI or infrared imaging requires the coupling of our results to a complete imaging pipeline such as the one employed by the EHT and GRAVITY collaborations. A detailed discussion of such rendering will be presented in a future work

## ACKNOWLEDGEMENTS

AN and VM were supported by the Hellenic Foundation for Research and Innovation (HFRI) under the 2nd Call for HFRI (Project Number: 00634). Support also comes from the ERC Advanced Grant “JETSET: Launching, propagation and emission of relativistic jets from binary mergers and across mass scales” (Grant No. 884631). The simulations were performed on SuperMUC at LRZ in Garching, on the GOETHE-HLR cluster at CSC in Frankfurt, and on the HPE Apollo Hawk at the High Performance Computing Center Stuttgart (HLRS) under the grant numbers BBHDISKS and BNSMIC.

## DATA AVAILABILITY

The data underlying this article will be shared on reasonable request to the corresponding author.

## REFERENCES

- Abuter R., et al., 2018, *Astron. Astrophys.*, 615, L15
- Baganoff F. K., et al., 2001, *Nature*, 413, 45
- Ball D., Özel F., Psaltis D., Chan C.-k., 2016, *Astrophys. J.*, 826, 77
- Ball D., Özel F., Psaltis D., Chan C.-K., Sironi L., 2018a, *Astrophys. J.*, 853, 184
- Ball D., Sironi L., Özel F., 2018b, *Astrophys. J.*, 862, 80
- Barkov M. V., Baushev A. N., 2011, *New Astronomy*, 16, 46
- Barrière N. M., et al., 2014, *Astrophys. J.*, 786, 46
- Begelman M. C., Fabian A. C., Rees M. J., 2008, *Mon. Not. R. Astron. Soc.*, 384, L19
- Bhattacharjee A., Huang Y.-M., Yang H., Rogers B., 2009, *Physics of Plasmas*, 16, 112102
- Broderick A. E., Loeb A., 2005, *Mon. Not. R. Astron. Soc.*, 363, 353
- Broderick A. E., Loeb A., 2006, *Mon. Not. R. Astron. Soc.*, 367, 905
- Broderick A. E., et al., 2016, *Astrophys. J.*, 820, 137
- Chan C.-K., Psaltis D., Özel F., Narayan R., Sądowski A., 2015, *Astrophys. J.*, 799, 1
- Chashkina A., Bromberg O., Levinson A., 2021, arXiv e-prints, p. arXiv:2106.15738
- Christie I. M., Lalakos A., Tchekhovskoy A., Fernández R., Foucart F., Quataert E., Kasen D., 2019, *Mon. Not. R. Astron. Soc.*, 490, 4811
- Del Zanna L., Zanotti O., Bucciantini N., Londrillo P., 2007, *Astron. Astrophys.*, 473, 11
- Del Zanna L., Papini E., Landi S., Bugli M., Bucciantini N., 2016, *Mon. Not. R. Astron. Soc.*, 460, 3753
- Dexter J., Agol E., Fragile P. C., 2009, *Astrophys. J.*, 703, L142
- Dexter J., et al., 2020, *Mon. Not. R. Astron. Soc.*, 494, 4168
- Dihingia I. K., Vaidya B., Fendt C., 2021, *Mon. Not. R. Astron. Soc.*, 505, 3596
- Dionysopoulou K., Alic D., Rezzolla L., 2015, *Phys. Rev. D*, 92, 084064
- Do T., et al., 2019, arXiv e-prints, p. arXiv:1908.01777
- Dodds-Eden K., et al., 2009, *Astrophys. J.*, 698, 676
- Dodds-Eden K., Sharma P., Quataert E., Genzel R., Gillessen S., Eisenhauer F., Forquet D., 2010, *Astrophys. J.*, 725, 450
- Doeleman S. S., et al., 2008, *Nature*, 455, 78
- Edmondson J. K., Lynch B. J., 2017, *Astrophys. J.*, 849, 28
- Event Horizon Telescope Collaboration et al., 2019a, *Astrophys. J. Lett.*, 875, L5
- Event Horizon Telescope Collaboration et al., 2019b, *Astrophys. J. Lett.*, 875, L6
- Event Horizon Telescope Collaboration et al., 2021a, *Astrophys. J. Lett.*, 910, L12
- Event Horizon Telescope Collaboration et al., 2021b, *Astrophys. J. Lett.*, 910, L13
- Falcke H., Goss W. M., Matsuo H., Teuben P., Zhao J.-H., Zylka R., 1998, *Astrophys. J.*, 499, 731
- Fermo R. L., Drake J. F., Swisdak M., 2010, *Physics of Plasmas*, 17, 010702
- Fishbone L. G., Moncrief V., 1976, *Astrophys. J.*, 207, 962
- GRAVITY collaboration Abuter R., et al., 2018, *Astron. Astrophys.*, 618, L10
- Genzel R., Schödel R., Ott T., Eckart A., Alexander T., Lacombe F., Rouan D., Aschenbach B., 2003, *Nature*, 425, 934
- Ghisellini G., Tavecchio F., 2008, *Mon. Not. R. Astron. Soc.*, 386, L28
- Giannios D., 2013, *Mon. Not. R. Astron. Soc.*, 431, 355
- Giannios D., Uzdensky D. A., 2019, *Mon. Not. R. Astron. Soc.*, 484, 1378
- Giannios D., Uzdensky D. A., Begelman M. C., 2009, *Mon. Not. R. Astron. Soc.*, 395, L29
- Goddi C., et al., 2021, *Astrophys. J. Lett.*, 910, L14
- Gravity Collaboration et al., 2020, *Astron. Astrophys.*, 635, A143
- Guo F., Li H., Daughton W., Liu Y.-H., 2014, *Phys. Rev. Lett.*, 113, 155005
- Guo F., Liu Y.-H., Daughton W., Li H., 2015, *Astrophys. J.*, 806, 167
- Guo F., Li X., Daughton W., Li H., Kilian P., Liu Y.-H., Zhang Q., Zhang H., 2021, *Astrophys. J.*, 919, 111
- Gutiérrez E. M., Nemmen R., Cafardo F., 2019, arXiv e-prints, p. arXiv:1912.10945
- Haggard D., et al., 2019, *Astrophys. J.*, 886, 96
- Huang Y.-M., Bhattacharjee A., 2012, *Phys. Rev. Lett.*, 109, 265002
- Igumenshchev I. V., Narayan R., Abramowicz M. A., 2003, *Astrophys. J.*, 592, 1042
- Johnson M. D., Gwinn C. R., 2015, *Astrophys. J.*, 805, 180
- Kadowaki L. H. S., De Gouveia Dal Pino E. M., Stone J. M., 2018, *Astrophys. J.*, 864, 52
- Kagan D., Nakar E., Piran T., 2018, *Mon. Not. R. Astron. Soc.*, 476, 3902
- Kumar P., Karpen J. T., Antiochos S. K., Wyper P. F., DeVore C. R., 2019, *Astrophys. J. Lett.*, 885, L15
- Lazarian A., Eyink G. L., Jafari A., Kowal G., Li H., Xu S., Vishniac E. T., 2020, *Physics of Plasmas*, 27, 012305
- Levinson A., 2007, *Astrophys. J. Letters*, 671, L29
- Li Y.-P., Yuan F., Wang Q. D., 2017a, *Mon. Not. R. Astron. Soc.*, 468, 2552
- Li X., Guo F., Li H., Li G., 2017b, *Astrophys. J.*, 843, 21
- Loureiro N. F., Schekochihin A. A., Cowley S. C., 2007, *Physics of Plasmas*, 14, 100703
- Loureiro N. F., Samtaney R., Schekochihin A. A., Uzdensky D. A., 2012, *Physics of Plasmas*, 19, 042303
- Mahlmann J. F., Levinson A., Aloy M. A., 2020, *Mon. Not. R. Astron. Soc.*, 494, 4203
- Markoff S., 2005, *Astrophys. J.*, 618, L103
- Marrone D. P., Moran J. M., Zhao J.-H., Rao R., 2007, *Astrophys. J.*, 654, L57
- Matsumoto T., Chan C.-H., Piran T., 2020, *Mon. Not. R. Astron. Soc.*, 497, 2385
- Mizuno Y., et al., 2018, *Nature Astronomy*, 2, 585
- Mizuno Y., Fromm C. M., Younsi Z., Porth O., Olivares H., Rezzolla L., 2021, *MNRAS*, 506, 741
- Narayan R., Sądowski A., Penna R. F., Kulkarni A. K., 2012, *Mon. Not. R. Astron. Soc.*, 426, 3241
- Nathanail A., Porth O., Rezzolla L., 2019, *Astrophys. J. Lett.*, 870, L20
- Nathanail A., Fromm C. M., Porth O., Olivares H., Younsi Z., Mizuno Y., Rezzolla L., 2020a, *MNRAS*, 495, 1549
- Nathanail A., Gill R., Porth O., Fromm C. M., Rezzolla L., 2020b, *Mon. Not. R. Astron. Soc.*, 495, 3780
- Obergaulinger M., Aloy M. A., 2020, in Journal of Physics Conference Series. p. 012018 (arXiv:2001.01927), doi:10.1088/1742-6596/1623/1/012018
- Obergaulinger M., Cerdá-Durán P., Müller E., Aloy M. A., 2009, *Astron. Astrophys.*, 498, 241
- Olivares H., Porth O., Davelaar J., Most E. R., Fromm C. M., Mizuno Y., Younsi Z., Rezzolla L., 2019, *Astron. Astrophys.*, 629, A61
- Olivares H., et al., 2020, *MNRAS*, 497, 521

- Parfrey K., Giannios D., Beloborodov A. M., 2015, *Mon. Not. R. Astron. Soc.*, **446**, L61
- Petropoulou M., Christie I. M., Sironi L., Giannios D., 2018, *Mon. Not. R. Astron. Soc.*, **475**, 3797
- Petropoulou M., Sironi L., Spitkovsky A., Giannios D., 2019, *Astrophys. J.*, **880**, 37
- Ponti G., et al., 2017, *Mon. Not. R. Astron. Soc.*, **468**, 2447
- Porth O., Olivares H., Mizuno Y., Younsi Z., Rezzolla L., Moscibrodzka M., Falcke H., Kramer M., 2017, *Computational Astrophysics and Cosmology*, **4**, 1
- Porth O., et al., 2019, *Astrophys. J. Supp.*, **243**, 26
- Porth O., Mizuno Y., Younsi Z., Fromm C. M., 2021, *Mon. Not. R. Astron. Soc.*,
- Qian Q., Fendt C., Vourellis C., 2018, *Astrophys. J.*, **859**, 28
- Reid M. J., 2009, *International Journal of Modern Physics D*, **18**, 889
- Rembiasz T., Obergaulinger M., Cerdá-Durán P., Aloy M.-Á., Müller E., 2017, *Astrophys. J., Supp.*, **230**, 18
- Ressler S. M., Quataert E., Stone J. M., 2018, *Mon. Not. R. Astron. Soc.*, **478**, 3544
- Rezzolla L., Zanotti O., 2013, *Relativistic Hydrodynamics*. Oxford University Press, Oxford, UK, doi:10.1093/acprof:oso/9780198528906.001.0001
- Ripperda B., et al., 2019a, *Astrophys. J., Supp.*, **244**, 10
- Ripperda B., Porth O., Sironi L., Keppens R., 2019b, *Mon. Not. R. Astron. Soc.*, **485**, 299
- Ripperda B., Bacchini F., Philippov A. A., 2020, *Astrophys. J.*, **900**, 100
- Ripperda B., Liska M., Chatterjee K., Musoke G., Philippov A. A., Markoff S. B., Tchekhovskoy A., Younsi Z., 2021, arXiv e-prints, p. arXiv:2109.15115
- Rowan M. E., Sironi L., Narayan R., 2017, *Astrophys. J.*, **850**, 29
- Rowan M. E., Sironi L., Narayan R., 2019, *Astrophys. J.*, **873**, 2
- Scepi N., Dexter J., Begelman M. C., 2021, arXiv e-prints, p. arXiv:2107.08056
- Shende M. B., Subramanian P., Sachdeva N., 2019, *Astrophys. J.*, **877**, 130
- Sironi L., Spitkovsky A., 2014, *Astrophys. J.*, **783**, L21
- Sironi L., Giannios D., Petropoulou M., 2016, *Mon. Not. R. Astron. Soc.*, **462**, 48
- Stanier A., Daughton W., Le A., Li X., Bird R., 2019, *Physics of Plasmas*, **26**, 072121
- Takamoto M., 2013, *Astrophys. J.*, **775**, 50
- Tchekhovskoy A., Narayan R., McKinney J. C., 2011, *Mon. Not. R. Astron. Soc.*, **418**, L79
- Uzdensky D. A., Loureiro N. F., Schekochihin A. A., 2010, *Phys. Rev. Lett.*, **105**, 235002
- Vourellis C., Fendt C., Qian Q., Noble S. C., 2019, *Astrophys. J.*, **882**, 2
- Werner G. R., Uzdensky D. A., Cerutti B., Nalewajko K., Begelman M. C., 2016, *Astrophys. J. Let.*, **816**, L8
- White C. J., Quataert E., Gammie C. F., 2020, *Astrophys. J.*, **891**, 63
- Witzel G., et al., 2018, *Astrophys. J.*, **863**, 15
- Wong G. N., Du Y., Prather B. S., Gammie C. F., 2021, arXiv e-prints, p. arXiv:2104.07035
- Younsi Z., Wu K., 2015, *Mon. Not. R. Astron. Soc.*, **454**, 3283
- Yuan F., Quataert E., Narayan R., 2003, *Astrophys. J.*, **598**, 301
- Yuan F., Lin J., Wu K., Ho L. C., 2009, *Mon. Not. R. Astron. Soc.*, **395**, 2183
- Yuan Y., Blandford R. D., Wilkins D. R., 2019a, *Mon. Not. R. Astron. Soc.*, **484**, 4920
- Yuan Y., Spitkovsky A., Blandford R. D., Wilkins D. R., 2019b, *Mon. Not. R. Astron. Soc.*, **487**, 4114
- Zhang Q., Guo F., Daughton W., Li H., Li X., 2021, *Phys. Rev. Lett.*, **127**, 185101
- Čemeljić M., Yuan F., Yang H., 2020, arXiv e-prints, p. arXiv:2012.00916